Journal of Materials Chemistry C

ROYAL SOCIETY OF CHEMISTRY

PAPER

View Article Online
View Journal

Cite this: DOI: 10.1039/d3tc02547k

Phase segregation affects electron–phonon coupling in perovskite solar cell materials

Ilhan Yavuz

Phase segregation has been described as a significant factor that limits solar cell efficiency and long-term stability in mixed organic–inorganic halide perovskite materials. It is often microscopically linked to the electron–phonon coupling when the device is under operation. Through computational calculations, Migdal-Eliashberg theory and the Fröhlich large polaron model, we examined the control of phase segregation, in bulk I/Br and FA/Cs mixtures, over the electron–phonon coupling strength. We revealed that either A-site or X-site phase segregation destabilizes the material but reduces the electron–phonon coupling and increases the charge carrier mobility. Segregation promotes higher frequency vibrations and phonon instability is generally caused by $[PbI_6]^{4-}$ octahedral torsions and liberations in FA^+. Phonon dispersion has stronger control over the electron–phonon coupling than electronic bands. We expect that our theoretical findings will influence future discussions regarding the interplay of phase segregation and electron–phonon interactions in perovskite solar cells.

Received 19th July 2023,
Accepted 8th October 2023

DOI: 10.1039/d3tc02547k

rsc.li/materials-c

Introduction

The perovskite structure is a class of material that has a general formula of ABX_3, where A and B are cations, and X is an anion, typically halides. Perovskite solar cells (PSCs) have recently emerged as a promising solar cell technology due to their high power conversion efficiency, low cost, and facile fabrication, which rivals that of traditional silicon-based solar cells. The high efficiency is primarily due to the high absorption coefficient and long carrier lifetime of perovskite materials. PSCs are often fabricated using facile solution processing techniques, making them highly scalable and cost-effective. PSCs also offer the potential for flexible and transparent devices, making them ideal for use in a variety of applications, including building-integrated photovoltaics and wearable electronics. Despite their major potential, PSCs face several challenges, including stability, the toxicity of lead-based perovskites, and reproducibility. The instability of perovskite materials in the presence of moisture and heat is a significant concern, limiting their long-term performance and durability.[1–8]

Formation of heterogeneous domains in material compositions and crystal phases, namely phase segregation, is a common phenomenon in "mixed" perovskite materials, with tunable band-gaps, that can significantly impact the electronic and optical properties.[9,10] Phase segregation can occur due to a variety of factors, including the presence of impurities or defects, changes in processing conditions, and exposure to external stimuli such as light or heat, *etc.* These factors can even interact with each other in subtle ways, leading to such behaviors that are difficult to predict or explain.[11,12] Studies have shown that the formation of these distinct domains within the perovskite material can lead to variations in the band structure, charge-carrier mobility, recombination dynamics, *etc.* Much effort has recently been devoted to preventing the formation of phase segregation, which is a crucial factor for photovoltaic device stability and performance. Defect passivation and doping have been proposed to mitigate the effects of phase segregation on device performance.[13–16] Specifically, reduction of electron–phonon (e–ph) coupling can suppress light-induced phase segregation (*vide infra*). Here, e–ph coupling, resulting from the interaction between the lattice vibrations and the active charge carriers, leads to the formation of polarons, which is a self-trapping phenomenon.[17] Several studies have shown that modifying the perovskite crystal structure, such as altering the A-site cation, halide content or introducing dopants, can alter the e–ph coupling strength and reduce the formation of polarons.[11] Despite the continuous efforts, our understanding of the fundamental mechanisms responsible for phase segregation has remained incomplete. Therefore, understanding and controlling phase segregation is essential for optimizing the performance of perovskite solar cells.

Through density functional theory (DFT) we studied the variation of electronic structure, stability and charge transport by X-site doping in inorganic $CsPb(I_{1-x}Br_x)_3$ (Cs: cesium, Pb: lead, Br: bromide, I: iodide) and A-site doping in hybrid organic–inorganic $FA_{1-y}Cs_yPbI_3$ (FA: formamidinium) perovskites. We employed two widely accepted methodologies Migdal–Eliashberg theory and the

Department of Physics, Marmara University, Ziverbey, Istanbul, 34722, Turkey. E-mail: ilhan.yavuz@marmara.edu.tr

Fröhlich large polaron model to deeply examine the e–ph coupling. We aimed to better understand the factors that influence composite perovskite materials' performance and stability, which have implications for their use in various opto-electronic applications.

Results

To quantify the e–ph coupling, we first calculated the Eliashberg spectral function, $\alpha^2F(\omega)$, of $CsPb(I_{1-x}Br_x)_3$, in which we considered pure $CsPbI_3$ (x = 0) and two configurations of Br-doped $CsPb(I_{2/3}Br_{1/3})_3$ (x = 1/3). In all cases we considered the cubic crystal phases. As shown in Fig. 1A, major contributions to $\alpha^2F(\omega)$ occur at relatively lower frequencies. However, the addition of Br causes an extension of $\alpha^2F(\omega)$ to higher frequencies. First, we found a value of λ = 0.64 eV e–ph coupling strength for $CsPbI_3$. Besides, we also calculated the e–ph coupling of $FAPbI_3$ and found a value of 0.85 (see SI). Our λ values are consistent with ref. 18 and 19. The λ value of $CsPbI_3$ is notably increased when doped with Br ions, as shown in Fig. 1B and C. In addition, the relative positions of Br ions also impact the e–ph coupling. That is, when Br ions are in a close proximity but distanced (at a distance of ~6 Å), and potentially screened by other sites, λ is found to be 7.68 eV (Fig. 1B). The λ value decreases roughly by a factor of two and becomes 4.21 eV when Br ions are in the nearest neighborhood (of ~4 Å) (Fig. 1C). Therefore, we deduced that clustering of Br ions reduces the e–ph coupling. For the sake of convenience, we will call the former case as "uni" for $CsPb(I_{2/3}Br_{1/3})_3$ and as "seg" for the latter, to refer to the "model" uniform (mixed) and segregated (demixed) I/Br distributions, respectively. We observed that, for $CsPbI_3$, the highest frequency mode is near 16 meV, which is the A_{1g} symmetric I–Pb–I bending mode, as shown by the phonon DOS in Fig. 1A. This is also, even though being slight, the ultimate contributing mode to e–ph coupling (see also Fig. 1A). The lowest of $CsPbI_3$ is the T_{2u} asymmetric translation mode at 1.1 meV. The large $\alpha^2F(\omega)$ peak around 11 meV is caused by electron's coupling to the E_u asymmetric bond stretching mode. For $CsPb(I_{2/3}Br_{1/3})_3$, as shown in Fig. 1B and C, halide diversity leads to continuous variations in phonon states and activates new modes, which, we observed, contributes to the e–ph coupling. For the uni case (Fig. 1B), the in-plane Pb–Br–Pb bond stretching mode at 1.2 meV causes strong e–ph coupling and high-frequency modes as high as 13 meV, from an orthogonal (and split) I–Pb–I and Br–Pb–Br bond stretching mode, contribute to e–ph coupling. For the seg case (Fig. 1C), however, the overall $\alpha^2F(\omega)$ function as well as low-frequency contributions are reduced, compared to the uni case (Fig. 1B). This time, high-frequency contributions to e–ph coupling shift to 14 meV, due to the electron's coupling to the parallel (and split) I–Pb–I and Br–Pb–Br out-of-plane A_g symmetric bond-stretching mode.

e–ph coupling predictions based on the Fröhlich large polaron model are useful to elaborate the controlling factors between the electronic band and phonon dispersion. In this section, we provide a more detailed analysis of e–ph coupling in the uniform and segregated I/Br halide mixtures. In addition, we were also able to calculate the e–ph coupling in FA/Cs A-site cation mixtures. In all pure, uniform and segregated property calculations, relatively large super-cells are considered. These structures are first relaxed at the SCAN-rvv10 level of theory, which introduced slight site-disorder, as shown in Fig. 2A and B. We observed that the sites have a similar degree of disorder for both the pure I ion and I/Br cases. The c/a ratio can be useful to quantify the tolerance factor (in such super-cells) and the level of strain due to the presence of Br ions (c/a = 1 and c/a < 1 corresponds to cubic and tetragonal lattice, respectively). We found that c/a is roughly unity for both $CsPbI_3$ and $CsPb(I_{0.85}Br_{0.15})_3$ with uniformly distributed Br ions. c/a becomes 0.98 when I/Br ions segregate.

SCAN-rvv10 calculated projected band-structures and band-gap of $CsPb(I_{1-x}Br_x)_3$ near the valence-band maxima are presented in Fig. 2C. The band-gap of $CsPbI_3$ is predicted to be ~1.5 eV. The experimental band-gap of cubic $CsPbI_3$ is known to be 1.73 eV.[20] Apart from the computational accuracy, we also attribute the lower predicted band-gap to the tiny deviation from the cubic towards the tetragonal structure, which is known to lower the band-gap.[20] We observed that a small amount of Br ion addition to $CsPb(I_{1-x}Br_x)_3$ (*i.e.*, x = 0.012 case) increased the band-gap by 1.8%. However, we observed that in the case of 15% Br and 85% I mixture, *i.e.* $CsPb(I_{0.85}Br_{0.15})_3$, the band-gap is reduced compared to $CsPbI_3$.

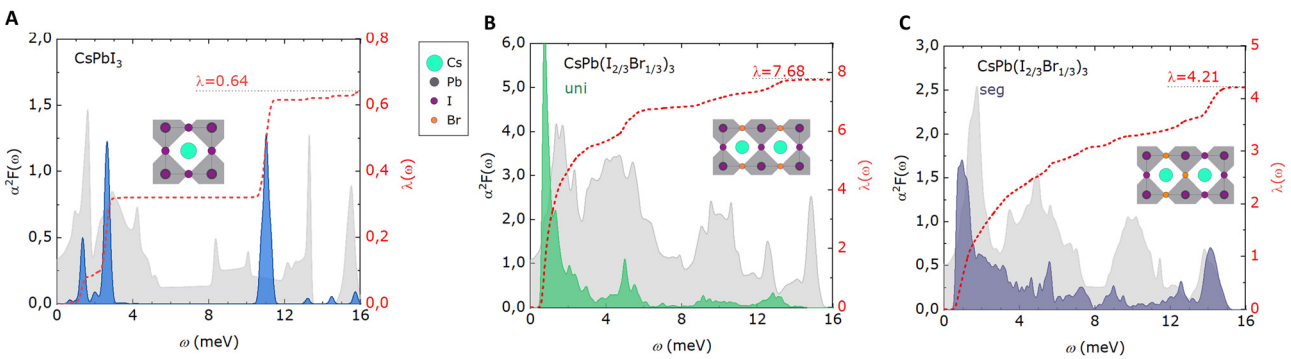

Fig. 1 Phonon density of states (grey areas) and phonon frequency resolved Eliashberg spectral function $\alpha^2F(\omega)$ (coloured areas) and cumulative electron–phonon coupling strength $\lambda(\omega)$ (red dashed lines) of A. $CsPbI_3$ and B and C. I/Br mixed $CsPb(I_{1-x}Br_x)_3$.

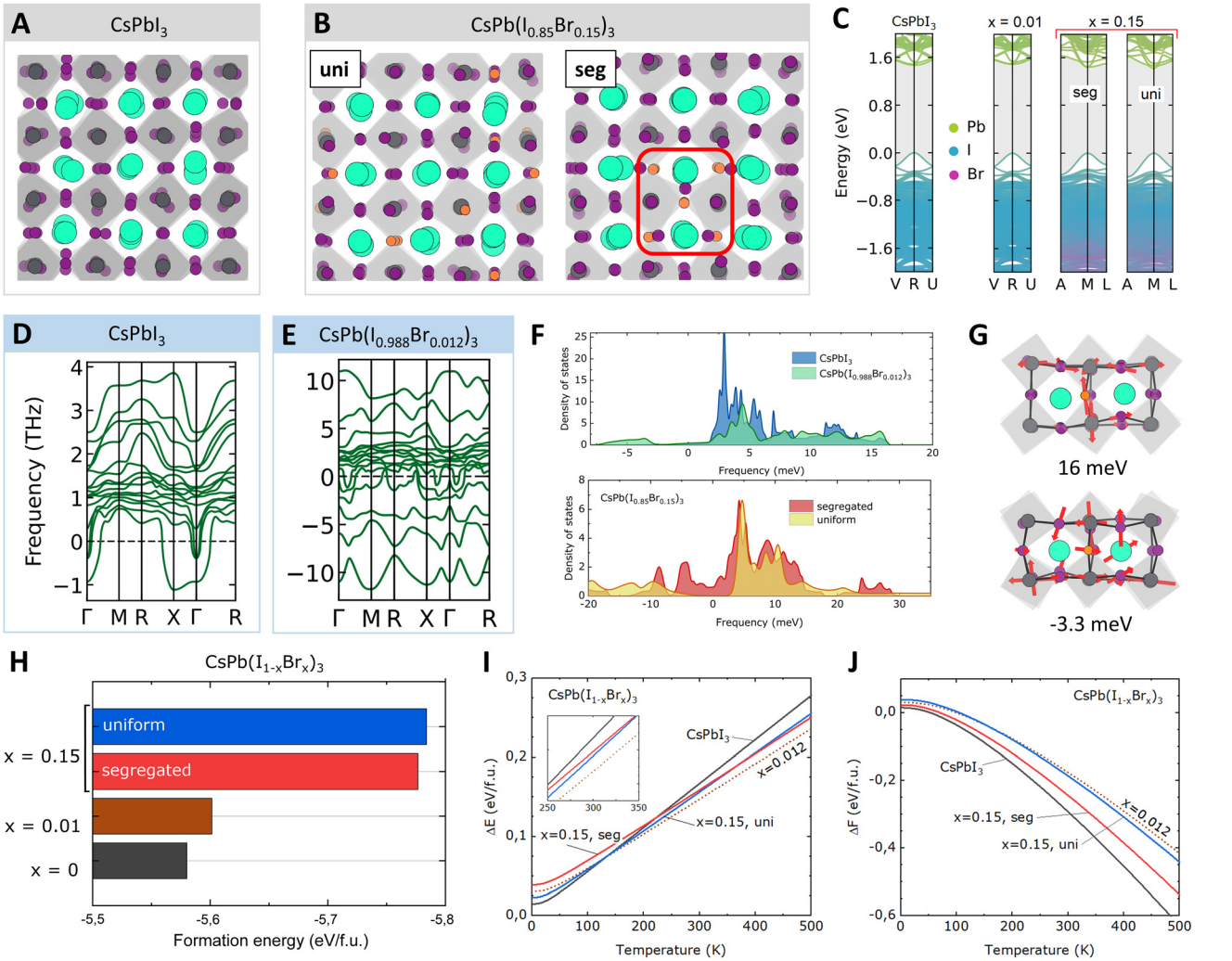

Fig. 2 Optimized structures of A. $CsPbI_3$ and B. uniform and segregated $CsPb(I_{0.85}Br_{0.15})_3$ mixed perovskites. The locations of Br ions are indicated by the red box. C. Band-structures of pure and Br ion-doped $CsPb(I_{1-x}Br_x)_3$ near the valence band maximum. D and E. Phonon dispersion relations. F. Total phonon DOS distributions. G. Phonon modes of $CsPb(I_{0.988}Br_{0.012})_3$ at two selected frequencies. H. Bar charts of formation energies of pure and Br ion-doped $CsPb(I_{1-x}Br_x)_3$. Temperature dependence of I. phonon energy of formation and J. Helmholtz free-energy of formation.

Projected band-structures in Fig. 2C show that Br ions mainly contribute to low energy valence bands. There are also notable variations in the band-gap in the case of uniform and segregated I/Br halide distributions. Compared to $CsPbI_3$, the band gap of uniform $CsPb(I_{0.85}Br_{0.15})_3$ is lowered by 3.0%, whereas that of segregated $CsPb(I_{0.85}Br_{0.15})_3$ is lowered by 1.6%. Effective masses of hole (m_h^*) and electron (m_e^*) transport were also predicted from the band-structures (see Table 1). Compared to $CsPbI_3$, the m_h^* effective mass of uniform $CsPb(I_{0.85}Br_{0.15})_3$ increased from 0.129 to 0.190, whereas the m_e^* effective mass increased only slightly; from 0.177 to 0.180. However, in both cases, increasing the hole effective-mass results in a reduction in hole transport. We found that segregation in $CsPb(I_{0.85}Br_{0.15})_3$ causes a slight increase in m_h^* (from 0.190 to 0.196) and decrease in m_e^* (from 0.180 to 0.166). Phonon dispersion of $CsPbI_3$ extends up to 16 meV and exhibits many branches, since we took a large (and disordered) super-cell into account (Fig. 2D). We observed that a small amount of Br ion dramatically changes the phonon dispersion (Fig. 2E). We observed phonon modes at as high as 46 meV, but they have

Table 1 Hole (m_h^*) and electron (m_e^*) effective masses (in m_0 units), phonon energy $(\hbar\omega_{LO})$ of the main LO mode (in meV units), hole (α_h) and electron (α_e) Fröhlich coupling constant and calculated hole (μ_h) and electron (μ_h) mobilities (in $cm^2\ V^{-1}\ s^{-1}$ units). u: uniform and s: segregated mixtures

Compound	m_h^*	m_e^*	$\hbar\omega_{LO}$	α_h	α_e	μ_h	μ_e
$CsPbI_3$	0.129	0.177	16	1.23	1.45	64	40
$CsPb(I_{0.988}Br_{0.012})_3$	0.220	1.110	16	1.89	4.24	25	2
$CsPb(I_{0.85}Br_{0.15})_3$, u	0.190	0.180	21	1.53	1.49	37	40
$CsPb(I_{0.85}Br_{0.15})_3$, s	0.196	0.166	28	1.35	1.24	44	57
$FA_{0.11}Cs_{0.89}PbI_3$, u	0.169	0.875	11	1.68	3.34	37	7
$FA_{0.11}Cs_{0.89}PbI_3$, s	0.156	0.188	15	1.62	1.78	40	17
$FAPbI_3$	0.137	0.121	14	1.33	1.25	56	67
$MAPbI_3$	0.212	0.211	13	1.90	1.89	25	25

no effect on charge transport, evident from the phonon DOS shown in Fig. 2F. Namely, the maximum notable contributing frequency of both $CsPbI_3$ and $CsPb(I_{0.988}Br_{0.012})_3$ is at 16 meV. In contrast, a few high negative (imaginary) frequencies appear in $CsPb(I_{0.988}Br_{0.012})_3$ even though their contributions are small (Fig. 2E and F). As shown in Fig. 2G, vibrations at 16 meV (longitudinal optical, LO, mode) are A_{1g}-like, whereas, for instance, a negative vibration at 3.3 meV is an octahedral torsion (*i.e.*, F_{2g}). Uniform I/Br mixed $CsPb(I_{0.85}Br_{0.15})_3$ perovskite exhibits extended LO phonon frequencies up to 21 meV (Fig. 2F), but in addition, promotes vibrational instabilities due to strong phonon DOS at negative frequencies. When the I/Br mixture in $CsPb(I_{0.85}Br_{0.15})_3$ is segregated, the maximum frequency further increased to 28 meV. This is beneficial considering that $\alpha \propto 1/\omega_{LO}$. Relatively light atomic-weights of the Br ions and shorter Pb–Br distance (relative to that of Pb–I) contributes to increasing frequency in Br ion doped perovskite. In order to quantify this, we performed gas-phase DFT vibrational analysis on PbI_2, PbIBr and $PbBr_2$ at the B3LYP/def2-svp level using the ORCA package.[21] We saw that the gas-phase Pb-X (X = I, Br) stretching modes in PbI_2, PbIBr and $PbBr_2$ are 21.2, 25.7 and 25.9 meV, respectively.

Table 1 lists the electron and hole transport effective masses, LO mode frequencies and corresponding Fröhlich e–ph coupling (α) values for holes and electrons. We found $\alpha_h = 1.23$ and $\alpha_e = 1.45$ for $CsPbI_3$. Br ion doping increased the α values.[22] We found that in the case of uniform I/Br mixed $CsPb(I_{0.85}Br_{0.15})_3$ perovskite, the α values are increased relative to $CsPbI_3$ and become $\alpha_h = 1.53$ and $\alpha_e = 1.49$. However, compared to the uniform case, e–ph coupling, α, of holes and electrons are both reduced ($\alpha_h = 1.35$ and $\alpha_e = 1.24$) in the case of the segregated I/Br mixture in $CsPb(I_{0.85}Br_{0.15})_3$. Here, the reduction in e–ph coupling with phase segregation predicted by the Fröhlich polaron model is qualitatively consistent with our earlier e–ph coupling predictions from the Migdal–Eliashberg theory. Room-temperature hole and electron mobilities predicted based on the Fröhlich polaron model[18] for different compounds and mixtures are also shown in Table 1. Our predicted mobilities are typically on the order of 30–40 $cm^2\ V^{-1}\ s^{-1}$, consistent with the space-charge-limited current (SCLC) measurements for perovskite materials.[23,24] Specifically, phase segregated $CsPb(I_{0.85}Br_{0.15})_3$ have higher hole and electron mobilities ($\mu_h = 44$ and $\mu_e = 57\ cm^2\ V^{-1}\ s^{-1}$) compared to the uniform case ($\mu_h = 37$ and $\mu_e = 40\ cm^2\ V^{-1}\ s^{-1}$).

Formation energies, ΔH, calculated from the electronic states of pure and Br ion doped $CsPb(I_{1-x}Br_x)_3$ are predicted (Fig. 2H). The formation energy of pure $CsPbI_3$ ($x = 0$) is predicted to be −5.580 eV per f.u. (f.u.: formula unit) and $CsPbI_3$ is stabilized by Br ion doping. For an I/Br mixture with very low Br ion content (*i.e.*, $x = 0.012$), the formation energy is reduced to −5.602 eV per f.u. A uniform I/Br mixture, for $x = 0.15$, stabilized the perovskite even further to −5.784 eV per f.u. However, in the case of segregated I/Br with the same $x = 0.15$, the perovskite is destabilized (−5.777 eV per f.u.) compared to the uniform I/Br.

Temperature dependence of thermal energy differences in perovskite formation (energy ΔE of formation and Helmholtz

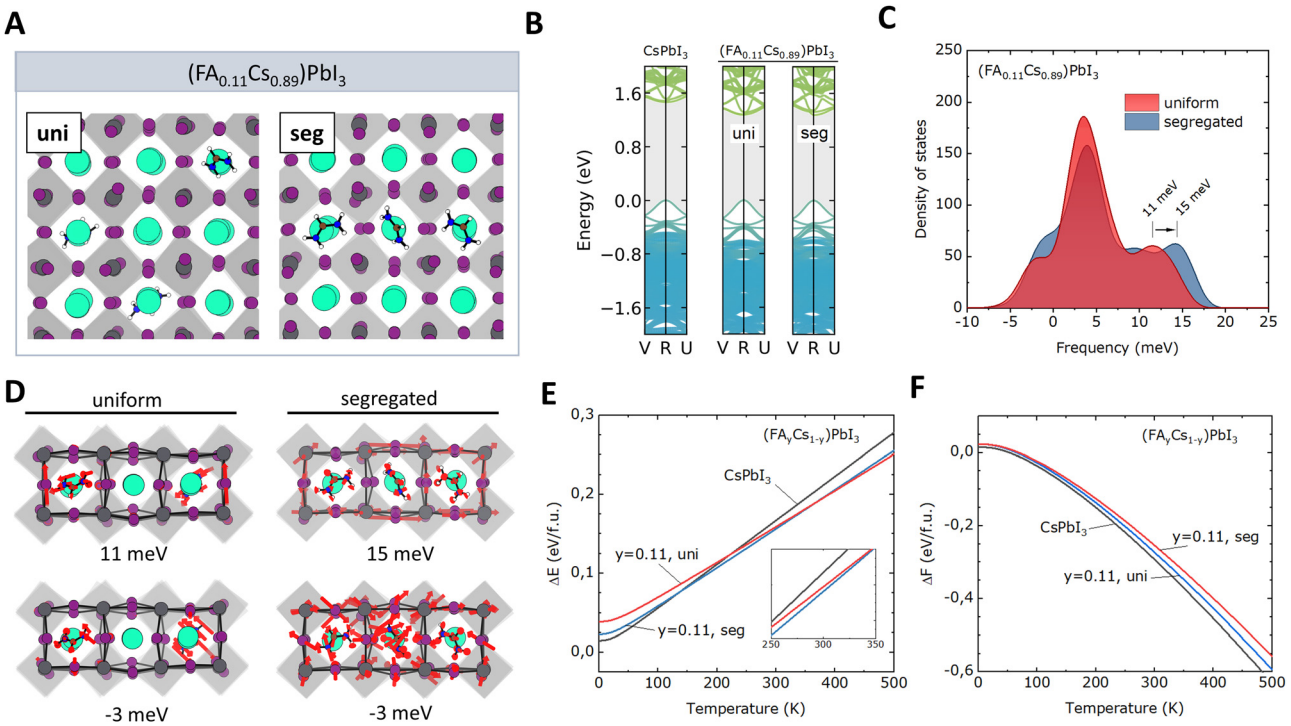

Fig. 3 Results for uniform and segregated FA/Cs mixture of $(FA_{0.11}Cs_{0.89})PbI_3$. A. Optimized structures. B. Band-structures near the valence band maximum. C. Total phonon DOS distributions. D. Phonon modes at two selected frequencies. Temperature dependence of E. phonon energy of formation and F. Helmholtz free-energy of formation.

free-energy ΔF of formation) from harmonic phonon modes are predicted in Fig. 2I and J. Here by ''formation'', we refer to the formation of perovskite material from its constituent elements in their stable states. In all cases, ΔE is increased and ΔF is decreased with increasing temperature due to entropic contributions, where $\Delta E = T\Delta S$ and $\Delta F = -S\Delta T$. At room-temperature (see the inset in Fig. 2I), ΔE of $CsPbI_3$ appears to be reduced by Br doping and for the $x = 0.15$ mixture, the segregated case is higher in ΔE than that of uniform. This indicates that phase segregation in I/Br thermally destabilizes the perovskite material. At any temperature (Fig. 2F), Br ion doping increases ΔF of $CsPbI_3$, whereas for the $x = 0.15$ mixture, phase segregation reduces ΔF compared to the uniform I/Br mixture.

In this section, we studied the phase segregation due to A-site FA/Cs mixtures and its effects on electronic structure, phonon dispersion, e–ph coupling and thermal properties. We considered $(FA_yCs_{1-y})PbI_3$ where $y = 0.11$ in our study. Fig. 3A depicts the case of a uniform FA/Cs mixture, where FA cations were randomly distributed and we made efforts to prevent them from being in their nearest neighbor A-sites as much as possible. In contrast, for the segregated case, we intentionally kept the FA cations in their nearest neighbor A-sites. The band-gap of uniform $(FA_{0.11}Cs_{0.89})PbI_3$ is less compared to that of $CsPbI_3$ and the band gap is reduced only 0.7% with FA/Cs segregation (Fig. 3B). The hole and electron effective masses are higher in both uniform and segregated $(FA_{0.11}Cs_{0.89})PbI_3$ compared to $CsPbI_3$ (see Table 1). However, we observed that with FA/Cs segregation, the hole and electron effective masses are reduced from 0.169 to 0.156 and from 0.875 to 0.188. Phonon dispersion of $(FA_{0.11}Cs_{0.89})PbI_3$ is shown in Fig. 3C. The high-frequency shoulder of uniform $(FA_{0.11}Cs_{0.89})PbI_3$ is at 11 meV and it shifts to 15 meV with phase segregation. As shown in Fig. 3D, I–Pb–I stretching modes coupled with the liberating FA modes are at 11 meV for the uniform and 15 meV for the segregation case, respectively. We saw that negative phonon vibrations at -3 meV are due to octahedral torsions coupled with the liberating FA. e–ph coupling strengths, α, of uniform and segregated $(FA_{0.11}Cs_{0.89})PbI_3$ calculated from the Fröhlich model are shown in Table 1. We also predicted the electronic and transport parameters of $FAPbI_3$ and $MAPbI_3$ (MA: methylammonium), as shown in Table 1, for benchmarking. We observed that α_h and α_e of uniform $(FA_{0.11}Cs_{0.89})PbI_3$ are increased to 1.68 and 3.34 compared to those of $CsPbI_3$, which are 1.23 and 1.45, respectively. However, α_h and α_e of $(FA_{0.11}Cs_{0.89})PbI_3$ reduced to 1.62 and 1.78 compared to the uniform case, respectively. This result is analogous to the reduction in e–ph coupling strength of $CsPb(I_{0.85}Br_{0.15})_3$ with phase segregation in I/Br mixtures. The formation energies of uniform and segregated $(FA_{0.11}Cs_{0.89})PbI_3$ are found to be -5.580 and -5.578 eV per f.u., respectively. The formation energy of $CsPbI_3$ was -5.580 eV per f.u. Therefore, we found that FA cations stabilize the $CsPbI_3$. However, we see that phase segregation destabilizes $(FA_{0.11}Cs_{0.89})PbI_3$ compared to the uniform case.

In summary, we investigate phase segregation in mixed organic–inorganic halide perovskite materials. Our goal was to gain a better understanding of the factors influencing the performance and stability of composite perovskite materials, which could be used in perovskite solar cells and opto-electronics. To examine the control of phase segregation, we used computational calculations, the Migdal–Eliashberg theory, and the Fröhlich large polaron model in bulk I/Br and FA/Cs mixtures. We revealed that A-site or X-site phase segregation destabilizes the material but reduces electron–phonon coupling and increases charge mobility. Based on the results shown in Table 1, we observed that the effective mass typically varies by 5–10% with phase segregation, whereas phonon energy $\hbar\omega_{LO}$ varies by roughly 25%. This suggests that phonon dispersion has a stronger influence over the electron–phonon coupling than electronic bands. We anticipate that our findings could influence future discussions about the interplay between phase segregation and electron–phonon interactions.

Method

All quantities in this paper are obtained entirely from first-principles calculations. The paper is composed of two main parts. For the first part, we calculated the e–ph coupling and its related quantities based on the Migdal–Eliashberg theory. For the second part, the Fröhlich large polaron model is employed to obtain the e–ph coupling elements and the related quantities are calculated accordingly.

I. We first examined the e–ph coupling using the maximally localized Wannier functions and Migdal–Eliashberg theory, as implemented in the Wannier90[25] and EPW[26] modules under the Quantum ESPRESSO (QE) code.[27] The strength of the e–ph interaction is described in terms of the Eliashberg spectral function $\alpha^2F(\omega)$ by

$$\alpha^2F(\omega) = \frac{1}{2}\sum_{\nu}\int\frac{d\mathbf{q}}{\Omega_{BZ}}\omega_{\mathbf{q}\nu}\lambda_{\mathbf{q}\nu}\delta(\omega-\omega_{\mathbf{q}\nu}) \quad (1)$$

where, $\omega_{q\nu}$ and $\lambda_{q\nu}$ are the phonon mode ν resolved frequency, q is the phonon wave-vector, and Ω_{BZ} is the volume of the first Brillouin zone. The cumulative e–ph coupling, $\lambda(\omega)$, is predicted from

$$\lambda(\omega) = 2\int_0^{\omega}\frac{d\omega}{\omega}\alpha^2F(\omega) \quad (2)$$

and the total e–ph coupling, λ, is obtained by taking $\omega \to \infty$.

For the quantum-mechanical calculations; to describe the core-valence interactions, we utilized norm-conserving pseudopotentials, while the PBE-type GGA functional was employed to describe the exchange and correlation energy within the framework of DFT. We ensured convergence of the total electronic energy to within 10^{-10} eV by using a $6 \times 6 \times 6$ Γ-centered k-mesh. For the phonon calculations we used the 10^{-14} eV convergence threshold and $2 \times 2 \times 2$ q-point mesh. A 544 eV kinetic energy cutoff is used for the plane-wave basis sets. To investigate the e–ph coupling, we considered interpolated $24 \times 24 \times 24$ mesh points in a k-grid and $12 \times 12 \times 12$ mesh points in a q-grid *via* Wannier functions. $CsPbI_3$ is used as the parent crystal and its experimental lattice parameters are used

in phonon dispersion and Eliashberg spectral function calculations.

II. For the second part, the Fröhlich large polaron model is studied for the e–ph coupling calculations. In this model, a parabolic electronic band with effective mass m^* couples to a LO mode with phonon energy $\hbar\omega_{LO}$, generating a quasi-particle called a polaron. The coupling strength is predicted by the dimensionless constant

$$\alpha = \frac{c_p e^2}{\hbar\varepsilon_0}\sqrt{\frac{m^*}{2\hbar\omega_{LO}}} \quad (3)$$

where $c_p = {\varepsilon_\infty}^{-1} - {\varepsilon_s}^{-1}$ is the Pekar factor, and ε_s and ε_∞ are the static and high-frequency dielectric constants, respectively. Hole and electron effective masses are used for α_h and α_e. Charge mobility can also be predicted from this model:

$$\mu = \frac{e}{m^*}\frac{\hbar}{\alpha k_B T}F(x) \quad (4)$$

where $x = \hbar\omega_{LO}/k_B T$ and an approximate $F(x)$ function in the form of $F(x) \simeq 0.052x^{3.3} + 0.34$, suggested in ref. 18, is used.

For this second part, the quantum-mechanical calculations are performed using the VASP code.[28,29] We used SCAN-rvv10[30,31] type *meta*-GGA with the vdW functional to describe the exchange–correlation. We employed the projector augmented wave method (PAW) for electron–core interactions.[32] We considered a cut-off energy of 400 eV for the plane-wave basis sets. Super-cells with a $3 \times 3 \times 3$ periodicity were used in all cases, in which experimental lattice parameters of $CsPbI_3$ are used to build the initial structures with or without doping. A 10^{-4} eV convergence threshold is used for electronic and phonon calculations. A structural relaxation for both ionic positions and cell dimensions is performed to obtain the optimized geometries until the residual forces become smaller than 0.01 eV $Å^{-1}$. Phonon dispersion relations and the static and high-frequency dielectric constants are predicted from density functional perturbation theory. Post-processing related to phonon calculation is performed using the Phonopy code.[33] Phonon energy of formation, $\Delta E(T)$, and free-energy of formation, $\Delta F(T)$, are predicted from the difference between the phonon energy of $CsPb(I_{1-x}Br_x)_3$ or $FA_yCs_{1-y}PbI_3$ mixed perovskites from its constituent elements in their stable states. bcc crystal phase for FA, hexagonal phase of Cs, fcc phase for Pb, and orthorhombic phases of I and Br are considered.

Conflicts of interest

The author declares no competing interests.

Acknowledgements

Computing resources were provided by the National Center for High-Performance Computing of Turkey (UHEM) under grant no: 1008342020.

References

1 Y. Zhao and K. Zhu, *Chem. Soc. Rev.*, 2016, **45**, 655–689.
2 H. J. Snaith, *Nat. Mater.*, 2018, **17**, 372–376.
3 J. J. Yoo, G. Seo, M. R. Chua, T. G. Park, Y. Lu, F. Rotermund, Y.-K. Kim, C. S. Moon, N. J. Jeon and J.-P. Correa-Baena, *et al.*, *Nature*, 2021, **590**, 587–593.
4 T. J. Jacobsson, A. Hultqvist, A. Garca-Fernández, A. Anand, A. Al-Ashouri, A. Hagfeldt, A. Crovetto, A. Abate, A. G. Ricciardulli and A. Vijayan, *et al.*, *Nat. Energy*, 2022, **7**, 107–115.
5 S. Tan, T. Huang, I. Yavuz, R. Wang, T. W. Yoon, M. Xu, Q. Xing, K. Park, D.-K. Lee and C.-H. Chen, *et al.*, *Nature*, 2022, **605**, 268–273.
6 E. Aydin, T. G. Allen, M. De Bastiani, L. Xu, J. Ávila, M. Salvador, E. Van Kerschaver and S. De Wolf, *Nat. Energy*, 2020, **5**, 851–859.
7 J. Y. Kim, J.-W. Lee, H. S. Jung, H. Shin and N.-G. Park, *Chem. Rev.*, 2020, **120**, 7867–7918.
8 J.-W. Lee, S. Tan, S. I. Seok, Y. Yang and N.-G. Park, *Science*, 2022, **375**, eabj1186.
9 D. J. Slotcavage, H. I. Karunadasa and M. D. McGehee, *ACS Energy Lett.*, 2016, **1**, 1199–1205.
10 A. D. Wright, C. Verdi, R. L. Milot, G. E. Eperon, M. A. Pérez-Osorio, H. J. Snaith, F. Giustino, M. B. Johnston and L. M. Herz, *Nat. Commun.*, 2016, **7**, 11755.
11 L. Tian, J. Xue and R. Wang, *Electron*, 2022, **11**, 700.
12 Z. Cui, Q. Zhang, Y. Bai and Q. Chen, *Mater. Chem. Front.*, 2023.
13 S. Ruan, M.-A. Surmiak, Y. Ruan, D. P. McMeekin, H. Ebendorff-Heidepriem, Y.-B. Cheng, J. Lu and C. R. McNeill, *J. Mater. Chem. C*, 2019, **7**, 9326–9334.
14 Y. Bai, Z. Huang, X. Zhang, J. Lu, X. Niu, Z. He, C. Zhu, M. Xiao, Q. Song and X. Wei, *et al.*, *Science*, 2022, **378**, 747–754.
15 L. A. Muscarella and B. Ehrler, *Joule*, 2022, **6**, 2016–2031.
16 Z. Wang, L. Zeng, T. Zhu, H. Chen, B. Chen, D. J. Kubicki, A. Balvanz, C. Li, A. Maxwell and E. Ugur, *et al.*, *Nature*, 2023, 1–3.
17 H. Fröhlich, *Adv. Phys.*, 1954, **3**, 325–361.
18 S. Poncé, M. Schlipf and F. Giustino, *ACS Energy Lett.*, 2019, **4**, 456–463.
19 J. Leveillee, G. Volonakis and F. Giustino, *J. Phys. Chem. Lett.*, 2021, **12**, 4474–4482.
20 G. E. Eperon, S. D. Stranks, C. Menelaou, M. B. Johnston, L. M. Herz and H. J. Snaith, *Energy Environ. Sci.*, 2014, **7**, 982–988.
21 F. Neese, *Wiley Interdiscip. Rev.: Comput. Mol. Sci.*, 2012, **2**, 73–78.
22 C. M. Iaru, A. Brodu, N. J. van Hoof, S. E. Ter Huurne, J. Buhot, F. Montanarella, S. Buhbut, P. C. Christianen, D. Vanmaekelbergh and C. de Mello Donega, *et al.*, *Nat. Commun.*, 2021, **12**, 5844.
23 Y. Yuan, G. Yan, R. Hong, Z. Liang and T. Kirchartz, *Adv. Mater.*, 2022, **34**, 2108132.
24 L. M. Herz, *ACS Energy Lett.*, 2017, **2**, 1539–1548.

25 G. Pizzi, V. Vitale, R. Arita, S. Blügel, F. Freimuth, G. Géranton, M. Gibertini, D. Gresch, C. Johnson and T. Koretsune, *et al.*, *J. Phys.: Condens. Matter*, 2020, **32**, 165902.
26 S. Poncé, E. R. Margine, C. Verdi and F. Giustino, *Comput. Phys. Commun.*, 2016, **209**, 116–133.
27 P. Giannozzi, S. Baroni, N. Bonini, M. Calandra, R. Car, C. Cavazzoni, D. Ceresoli, G. L. Chiarotti, M. Cococcioni and I. Dabo, *et al.*, *J. Phys.: Condens. Matter*, 2009, **21**, 395502.
28 G. Kresse and J. Hafner, *Phys. Rev. B*, 1993, **47**, 558.
29 G. Kresse and J. Furthmüller, *Comput. Mater. Sci.*, 1996, **6**, 15–50.
30 H. Peng, Z.-H. Yang, J. P. Perdew and J. Sun, *Phys. Rev. X*, 2016, **6**, 041005.
31 J. Klimeš, D. R. Bowler and A. Michaelides, *Phys. Rev. B: Condens. Matter Mater. Phys.*, 2011, **83**, 195131.
32 G. Kresse and D. Joubert, *Phys. Rev. B*, 1999, **59**, 1758.
33 A. Togo and I. Tanaka, *Scr. Mater.*, 2015, **108**, 1–5.